Supplementary information

Modelled glacier dynamics over the last quarter of a century at Jakobshavn Isbræ

Muresan et al.

Correspondence to: I. S. Muresan (iomur@space.dtu.dk)

1 The ice sheet model – parameters, sensitivity and seasonality

1.1 Parameters

Table S1. Ice sheet model parameters (The PISM Authors, 2014) that remain unchanged during the equilibrium and the forward simulations

Symbol	Description	Value
E_{SSA}	the flow enhancement factor for SSA	0.6
K	proportionality constant for eigen calving [ms]	2^{18}
ϕ	the till fraction angle*	°
ϕ_{min}	for bed elevations lower than 300 m below sea level [°]	15
ϕ_{max}	for bed elevations higher than 700 m above sea level [°]	40
S_0	salinity of the ocean water under the ice shelves [psu]	35

* The till fraction angle (ϕ) is computed as a piecewise-linear function of the bed elevation, with $\phi = 15°$ for bed elevations lower than 300 m below sea level, with $\phi = 40°$ for bed elevations higher than 700 m above sea level, and in between values with a linear change (see Eq. 8 in The PISM Authors (2014)).

Table S2. Ice sheet model parameters that have been altered from the default PISM values (The PISM Authors, 2014) during the forward simulations

Symbol	Description	Value*	Range**
E_{SIA}	the flow enhancement factor for SIA	1.2	1.0 - 1.3
F_{melt}	parameter for subshelf melting [$m\ s^{-1}$]	0.5505	0.01 - 1
H_{cr}	ice thickness threshold [m]	375	250 - 450
q	the exponent of the pseudo-plastic basal resistance model	0.25	0.2 - 0.3
δ	the till effective fraction overburden	0.02	0.01-0.03
T_o	temperature of the ocean water [$°C$]	-1.7	-1.3 - -1.9

* The parameterization that best captures the full evolution of JI during the period 1990–2014;

** Range (min/max values) for the parameters tested during the simulations;

The PISM parameters are described in detail by The PISM Authors (2014), Winkelmann et al. (2011) and Aschwanden et al. (2013). We perform over 50 simulations in which we vary during the regional runs different parameters with a focus on E_{SIA}, q, δ, F_{melt}, H_{cr} and T_o. The parameters or rather the range of the parameters (min, max) is shown in Table S2, 4th column. In order to match the overall retreat trend the parameters F_{melt}, H_{cr} and T_o were altered first. However, a finer tuning was required to match the observed front positions and to capture the two accelerations (i.e. 1998 and 2003) within the observed time frame. This fine tuning was done by altering some of the parameters that control ice dynamics (E_{SIA}, q, δ).

From the simulations, we present in the paper the parameterization that best captures the full evolution of JI during the period 1990–2014: (i) in terms of observed versus modelled front positions for 1990-2014 and (ii) based on the correlation between observed and modelled mass changes during 1997-2014. While (i) is based on our visual interpretation, for (ii) we selected those simulations within a +/- 30 Gt threshold. We found 3 simulations to satisfy (i) and (ii). From these simulations, we chose only the one that captures the two accelerations in the observational record within a 1 year time frame difference and that has overall magnitudes similar with those in the observational record (i.e. the RMSE in point S1 is ~2236 m a^{-1}; see also Fig. 3).

1.2 Sensitivity experiments for parameters controlling ice dynamics, basal processes and ice shelf melt

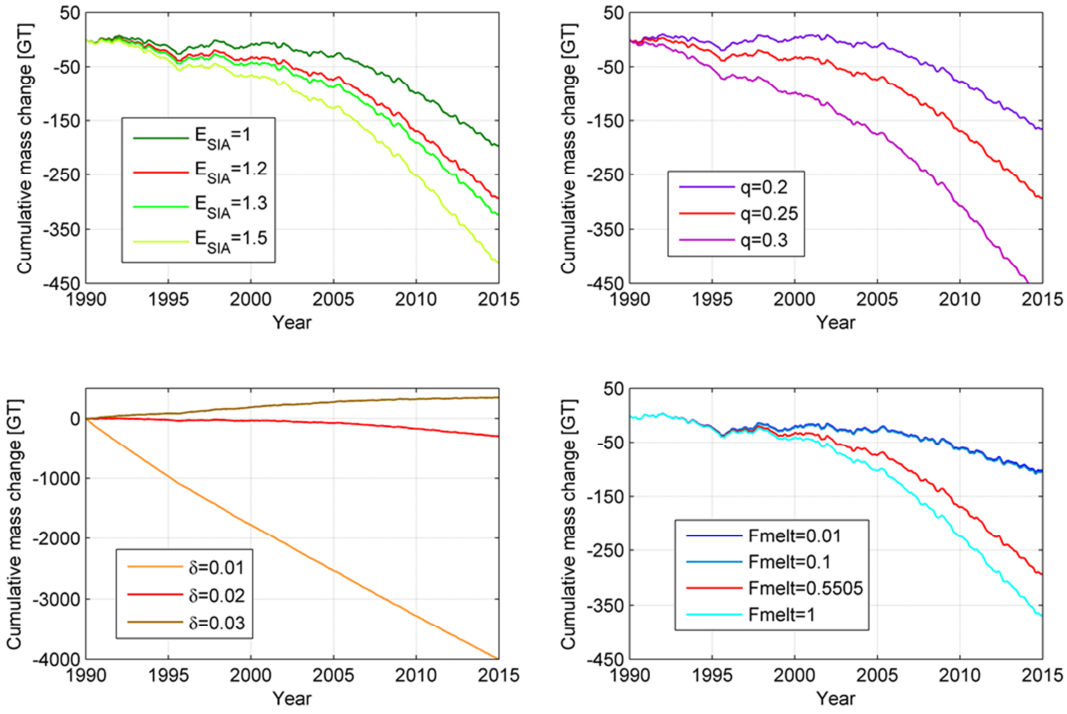

Figure S1. Sensitivity experiments for parameters controlling ice dynamics, basal processes and ice shelf melt. The curves for Fmelt=0.01 and Fmelt=0.1 are superimposed.

The parameterization that best captures the full evolution of JI during the period 1990–2014 is referred to as the reference run (red line in Fig. S1). The parameter values used during this simulation are included in Table S2 (3rd column).

1.2.1 Ice-flow enhancement factor for SIA

The first sensitivity experiment involves the SIA flow enhancement factor (E_{SIA}). The ice flow is governed by the effective viscosity of glacier ice as follows:

$$\eta = \frac{(\tau_e^2+\epsilon^2)^{\frac{1-n}{2n}}}{2E_{SIA}A} \qquad (1)$$

where τ_e^2 is the effective stress, ϵ is a constant (units of stress) which regularizes the flow law at low effective stress, n=3 is the exponent of the power law, E_{SIA} is the flow enhancement parameter for SIA, and A is the rate factor or the softness which is derived trough an enthalpy formulation (see Sect. 2.1).

The evolution in time of the cumulative mass change for different values of the flow enhancement factor is shown in Fig. S1 (top-left). The figure shows that for smaller values of the E_{SIA} (i.e. smaller than the reference run) the flow slows overall and therefore the modeled mass loss decreases as discharge decreases. The opposite behavior, i.e. flows accelerates and mass loss increases is seen for larger values of the E_{SIA}. A small delay in the terminus retreat (~1 year relative to the 2003 retreat from the reference run) is observed for E_{SIA}=1. The timing of the retreat is therefore sensitive to changes in E_{SIA}, while magnitude wise, it seems that the peaks and the flow accelerations modelled in the reference run (see Fig. 3) and dependent on the bed geometry (see Sect. 1.2.5 and Sect. 1.4) remain unaltered by changes in E_{SIA}.

1.2.2 The basal shear stress

The basal shear stress (τ_b) is related to the sliding velocity by a nearly-plastic power law (Schoof and Hindmarsh, 2010):

$$\tau_b = -\tau_c \frac{\boldsymbol{u}}{u_{threshold}^{q} |\boldsymbol{u}|^{1-q}} \qquad (2)$$

where τ_c is the till yield stress, $\boldsymbol{u}$ is the model sliding velocity, $u_{threshold}$= 100 m/yr represents the velocity threshold, and q is the exponent of the pseudo-plastic basal resistance model. Ice deforms as a result of basal shear stress and therefore, for values of q smaller than the reference run (see Fig. S1. top-right), the basal shear stress decreases making the mass loss and the terminus retreat to slow (e.g. +4 years relative to the 2003 retreat observed in the reference run). For values of q larger than the one used in the reference run, the basal shear stress increases making the mass loss and the terminus retreat accelerate (e.g. -4 years relative to the 2003 retreat observed in the reference run).

1.2.3 The yield stress

The Mohr-Coulomb criterion (Cuffey and Paterson, 2010) is used to relate the saturation, yield stress (τ_c), and the model liquid water within the till:

$$\tau_c = c_0 + \tan(\phi) N_{till} \qquad (3)$$

where c_0=0 kPa is the till cohesion, ϕ is the till fraction angle (see Table S2 for its values) and N_{till} is the effective pressure. The effective pressure on the till is determined by the modeled amount of water in the till:

$$N_{till} = \delta P_o 10^{(e_0/C_c)(1-(W_{till}/W_{till}^{max}))} \qquad (4)$$

where δ is the till effective fraction overburden, e_0=0.69 is the till reference void ratio, C_c =0.12 is the till compressibility coefficient, P_o is the ice overburden pressure, W_{till} is the effective thickness of water in the till computed by time-integrating the basal melt rate and W_{till}^{max} = 2 m is the maximum effective thickness of the water stored in the till. As seen in Fig. S1 (bottom-left), the model shows a high sensitivity relative to the value of the till effective fraction overburden used. The figure shows that for smaller values of δ (i.e. smaller than the reference run) the glacier grows in size and no retreat of the front is observed, while for larger values of δ the terminus retreat accelerates holding by 1998 the 2003 position observed in the reference run (i.e. -4 years relative to the 2003 reference run retreat).

1.2.4 F_{melt} – the model parameter

F_{melt} is a model parameter used in the heat flux equation and included in the parameterization for ice shelf melting (see Eq. 7). F_{melt} plays an important role in the terminus and groundling line retreat/ advance. As shown in Fig. S1 (bottom-right), smaller values of F_{melt} (i.e. smaller than in the reference run) result in low magnitude melt rates leading to a decrease in mass loss. The opposite behavior is encountered for larger values of F_{melt} (i.e. larger than the reference run). The magnitude of the melt rates increases and therefore the terminus and the grounding line retreat accelerates resulting in a mass loss increase.

1.2.5 Atmospheric forcing and ocean parametrization

Figures S2 and S3 denote the mean annual 2-meter air temperature and surface mass balance (SMB) for the computational domain shown in Fig. 1B and near the 2014 JIs terminus (as taken from RACMO 2.3 (Noël et al., 2015)). The data suggest an overall increase in temperature and a decrease in SMB. The decrease in SMB is most significant near the terminus. Overall 1996, 2010 and 2012 are characterized by higher mean annual temperatures.

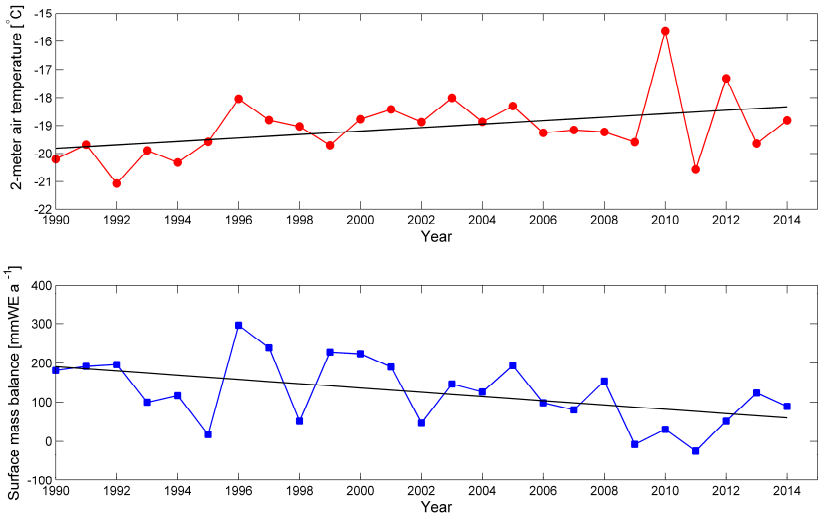

Figure S2. Mean annual 2-meter air temperature [°C] and surface mass balance [mmWE a^{-1}] with their respective trend lines (black line) during the period 1990-2014 for the computational domain shown in Fig. 1B (red border polygon). Note the lack of major changes (i.e. SMB and temperature) for 2012 relative to previous years.

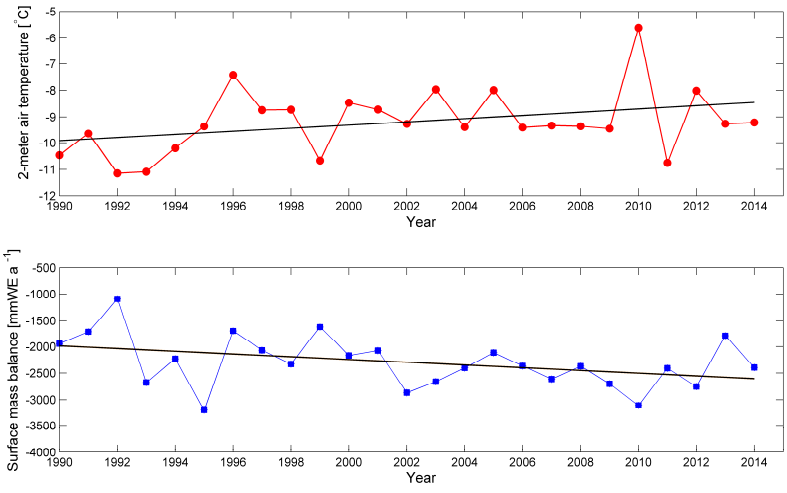

Figure S3. Mean annual 2-meter air temperature [°C] and surface mass balance [mmWE a^{-1}] (near the 2014 JIs terminus) with their respective trend lines (black line) for the period 1990-2014. Note the lack of major changes (i.e. SMB and temperature) for 2012 relative to previous years.

In the parametrization for ice shelf melting the melting effect of the ocean is based on both sub-shelf ocean temperature and salinity (Martin et al., 2011). At the base of the ice shelf, the sub-shelf ice temperature (T_{pm}) holds the following form:

$$T_{pm} = 273.15 + \beta_{cc} z_b \qquad (5)$$

where $\beta_{cc} = 8.66 \times 10^{-4}$ K m^{-1} represents the Clausius-Clapeyron gradient and z_b represents the elevation at the base of the ice shelf.

This mass flux from shelf to ocean (S) follows Beckmann and Goosse (2003) and is computed as a heat flux (Q_{heat}) between the ocean and ice that represents the melting effect of the ocean through both temperature and salinity (Martin et al., 2011):

$$S = \frac{Q_{heat}}{L_i \rho_i} \qquad (6)$$

$$Q_{heat} = \rho_o c_{p_o} \gamma_T F_{melt} (T_o - T_f) \qquad (7)$$

where $L_i = 3.35 \times 10^5$ J kg^{-1} is the latent heat capacity of ice, $c_{p_o} = 3974$ J (kg K)$^{-1}$ is the specific heat capacity of the ocean mixed layer, $\gamma_T = 10^{-4}$ m s^{-1} is the thermal exchange velocity, F_{melt} is a model parameter (see SI, Table S2), T_o is the ocean water temperature and T_f is the virtual temperature. This virtual temperature represents the freezing temperature of ocean water at the depth z_b below the ice shelf and has the form:

$$T_f = 273.15 + 0.0939 - 0.057 S_o + 7.64 \times 10^{-4} z_b \qquad (8)$$

where S_o is the salinity of the ocean.

For the simulations that best captures the full evolution of JI during the period 1990–2014 (red line in Figs. S5, the input ocean temperature (T_o) is set to a constant value of -1.7 °C. Although the input ocean temperature is constant, the heat flux supplied to the shelf is not constant in time and varies through T_o-T_f (see Eq. 5-8) based on the geometry of the shelf (see Fig. S4).

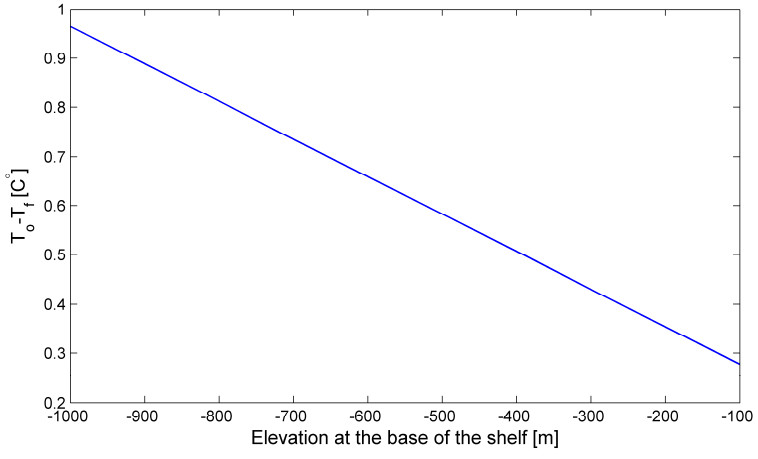

Figure S4. Ocean temperatures at the ice shelf base (T_o-T_f) illustrated for different possible elevations at the base of the shelf.

Fig. S5 shows the cumulative mass change at JI during the period 1990–2014 for different forcing combinations. Our results suggest that overall the atmospheric forcing (see Fig. S5, yellow, blue and red lines) plays a secondary role in JIs retreat (relative to the oceanic forcing). Compared with a simulation with ocean and monthly atmospheric forcing, in a simulation with constant climate (Figs. S5-blue line and S14), the retreat of the terminus relative to the 2003 retreat observed in the reference run is delayed by 1 year.

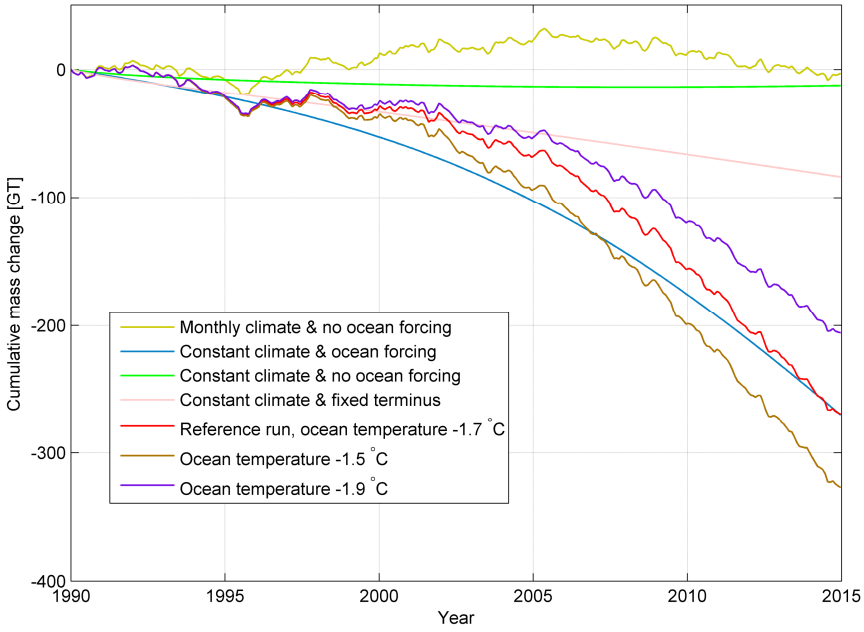

Figure S5. Cumulative mass change at JI during the period 1990–2014 for different forcing combinations. Monthly climate refers to a forcing with 1990-2014 monthly temperature and SMB as taken from RACMO2.3 (Noël et al., 2015). During the so called "constant climate" run (blue line) the monthly atmospheric forcing consists of mean 1960-1990 temperature and SMB (RACMO2.3, Noël et al., 2015). During the "no ocean" runs the parameterization for ice shelf melting is turned off (yellow and dark green lines). During the fixed terminus run (light pink line) the front is held fixed to the 1990 observed position. The cumulative mass change at JI for different ocean temperatures is shown with brown (-1.5 °C), red (-1.7 °C) and purple (-1.9 °C) lines. The reference run (red line) refers to the simulation that best captures the full evolution of JI between 1990-2014.

As shown in Fig. S5, the overall oceanic contribution to JIs retreat is significant and a simulation with no oceanic forcing results in a small growth of the glacier (see yellow line in Fig. S5) rather than a retreat. As depicted from Fig. S5 the model is sensitive to changes in ocean temperature. In our model, a decrease in ocean temperature of 0.2 °C is equivalent to a decrease in mass loss of ~70 Gt as the magnitude of the melt rate decreases and the retreat of the terminus slows (e.g. in the simulation with

T_0=- 1.9 °C, the 2003 retreat modelled in the reference run occurs only in 2014). On the other hand, an increase in ocean temperature is equivalent to an increase in mass loss (Fig. S5) as the retreat of the terminus accelerates.

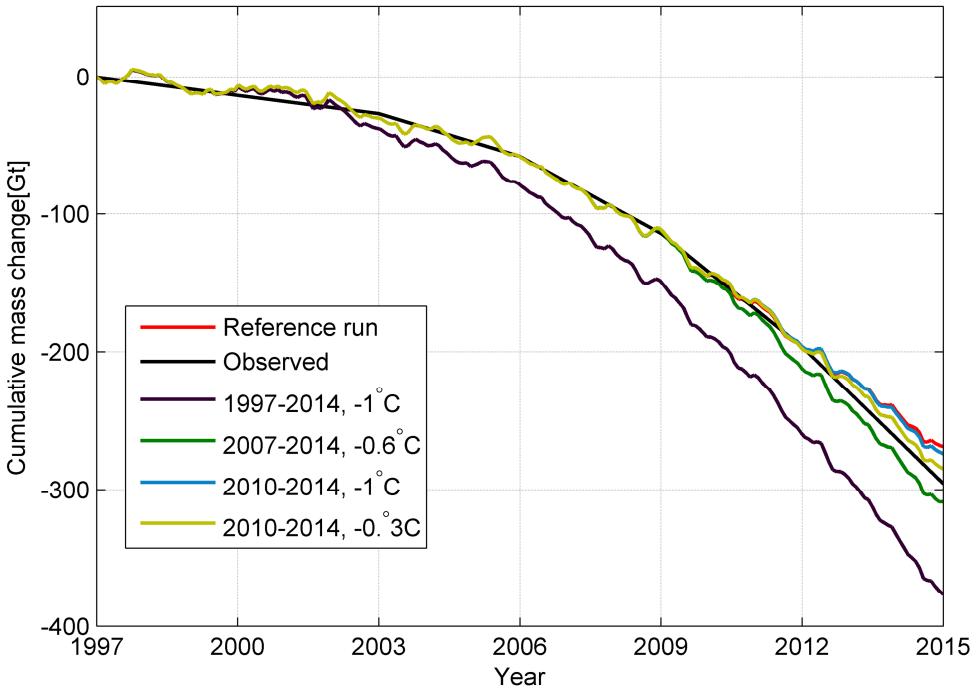

Figure S6. Cumulative mass change at JI for different ocean temperature experiments. In the experiment indicated by a dark green line, the reference ocean temperature (-1.7 °C) is adjusted from 2007-2014 with +1.1 °C, where +1.1 °C represents the mean surface ocean temperature between 2007 and 2014 (Gladish et al. 2015). In the experiment represented by the light blue line, the reference ocean temperature (-1.7 °C) is adjusted from 2010-2014 with +0.7 °C. In the remaining two experiments the input ocean temperature is adjusted starting 1997 (dark purple line) and 2010 (dark yellow line) with ocean temperature change calculated relative to 1990s (Gladish et al. 2015). These two experiments are consistent with observations of ocean temperature at the mouth of the Ilulissat fjord (Gladish et al. 2015). The curves for the reference run (red line), the "2010-2014, -1°C" experiment (light blue) and the "2010-2014, -0.3°C" experiment (dark yellow) are superimposed for the period 1990-2010. Note the large mass loss modelled in the experiment "1997-2014, -1°C" (dark purple line).

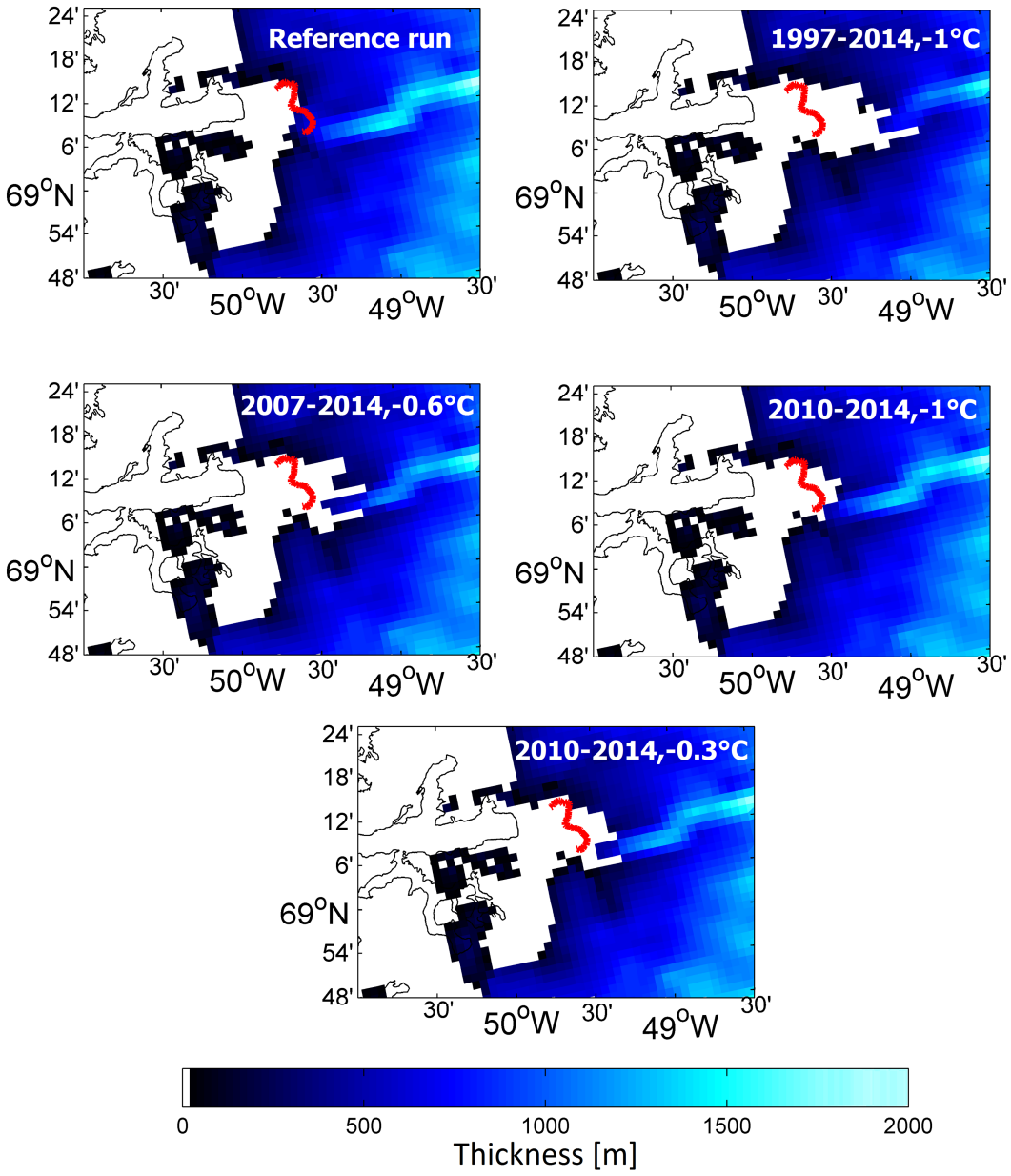

Figure S7. Terminus positions at the end of the forward run corresponding to December 2014 for the experiments introduced in Fig. S6 above. The red line represents the observed 2014 terminus position. Note the large terminus retreat for the experiment "1997-2014, -1°C" (top-right).

1.2.6 Grounding line, terminus position and deviatoric stresses

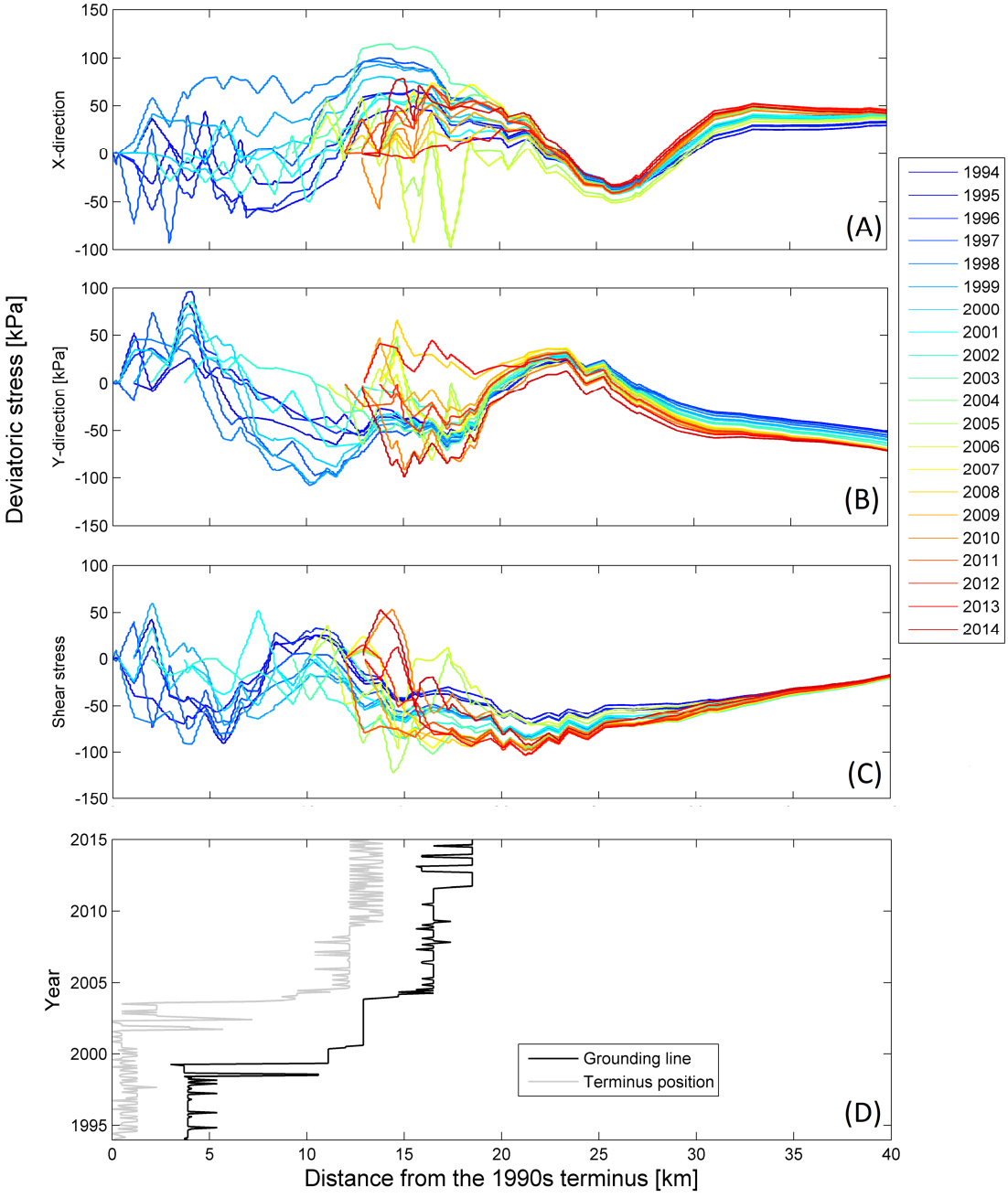

Figure S8. (A) Modelled 2D deviatoric stresses for the month of December during different years along the flow-line shown in Fig. 1C. (A) In the X direction, (B) in the Y direction, and (C) the shear stress.

The color scale ranges from dark blue (1994), light blue, green, yellow to red (2014) (see the legend on the right side of the figure). (D) Modelled grounding line and terminus position (ice thickness > 0) for the period 1994-2014.

1.2.8 Calving and basal melt rates

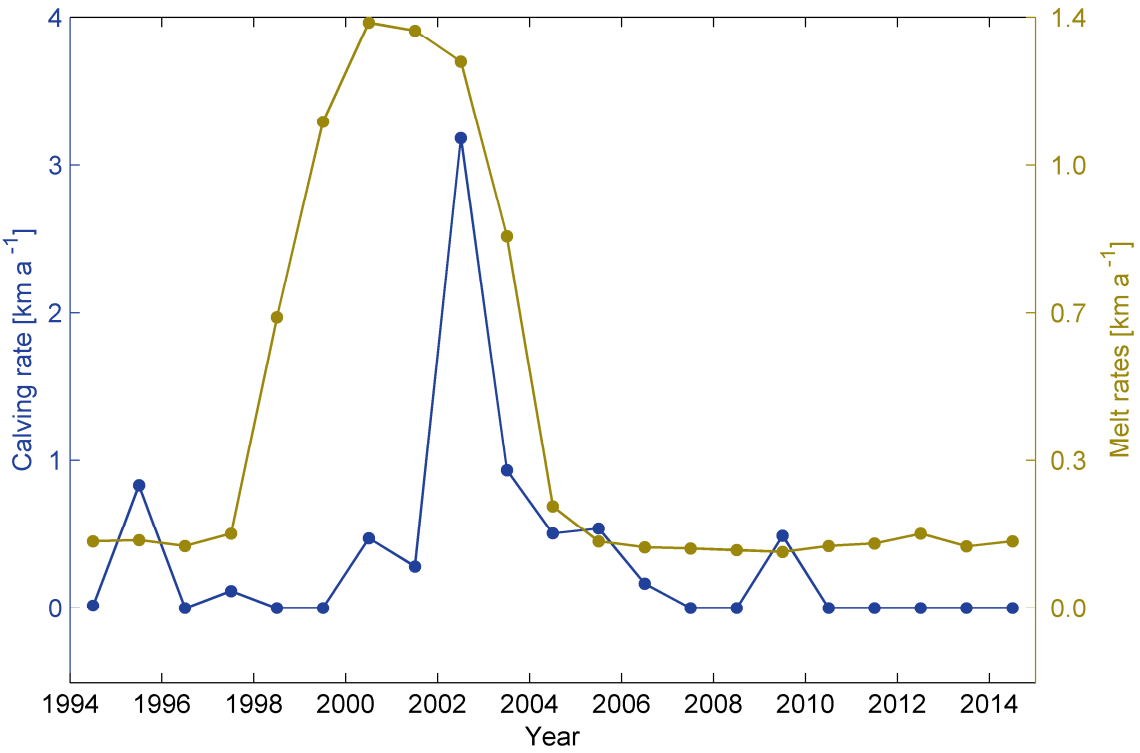

Figure S9. Mean calving rates versus mean basal melt rates for the period 1994-2014 in km a^{-1}.

Note the 1995 and 2010 accelerations in calving rate which do not correlate with an increase in basal melt rates.

1 Table S3. Mean yearly modelled basal melt rates.

Year	Melt rates [m/yr]
1990	262
1991	473
1992	150
1993	123
1994	159
1995	162
1996	148
1997	177
1998	690
1999	1153
2000	1387
2001	1368
2002	1295
2003	881
2004	242
2005	159
2006	145
2007	142
2008	138
2009	134
2010	148
2011	154
2012	177
2013	147
2014	159

2

3

4

5

6

7

8

1.3 Grid size and bedrock topography

1.3.1 Grid size

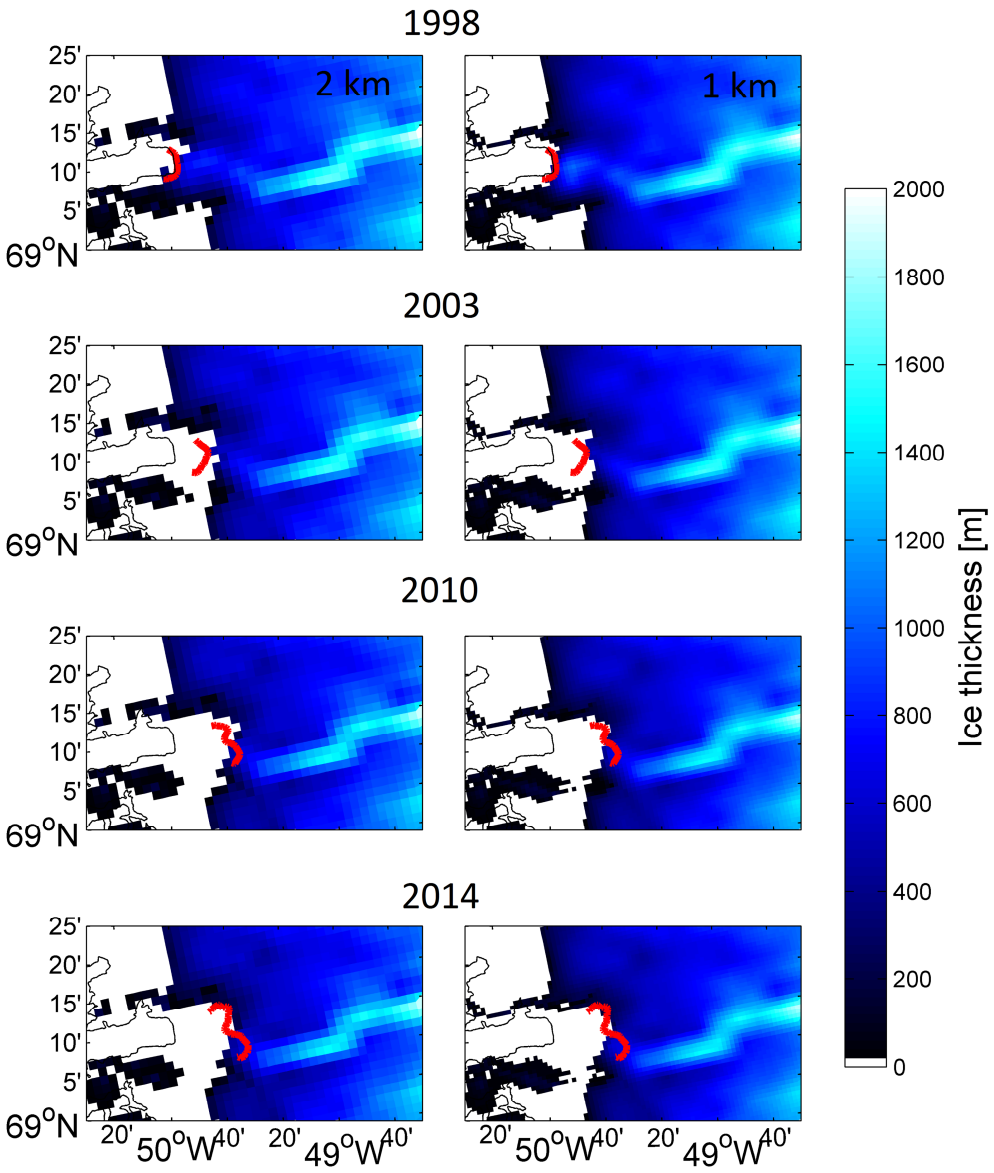

Figure S10. Modelled ice thickness at JI on a 2 km (left) and a 1 km (right) grid. The solid red lines represent the observed positions of the terminus for the different years plotted.

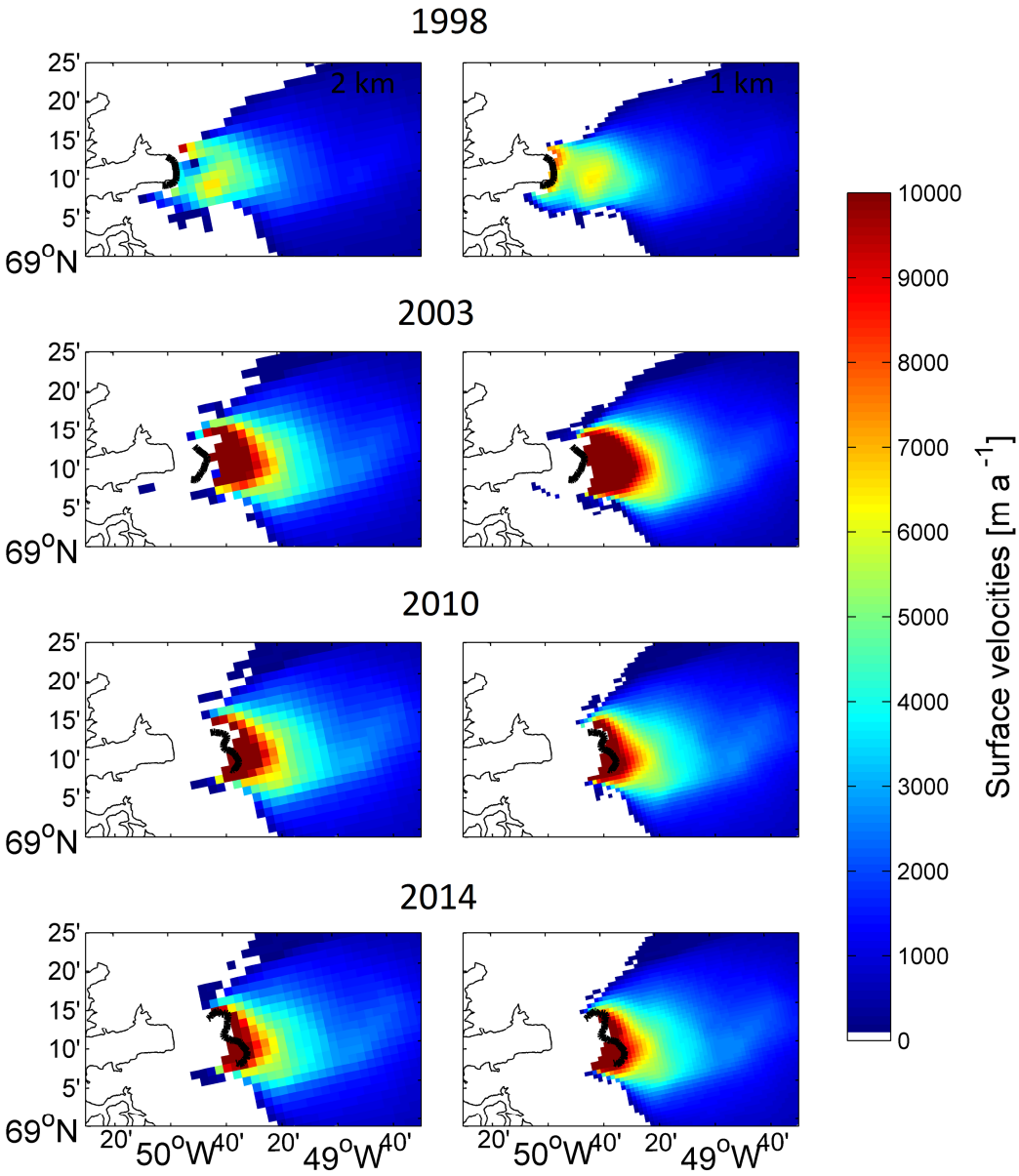

Figure S11. Modelled horizontal surface velocities at JI on a 2 km (left) and a 1 km (right) grid. The solid red lines represent the observed positions of the terminus for the different years plotted.

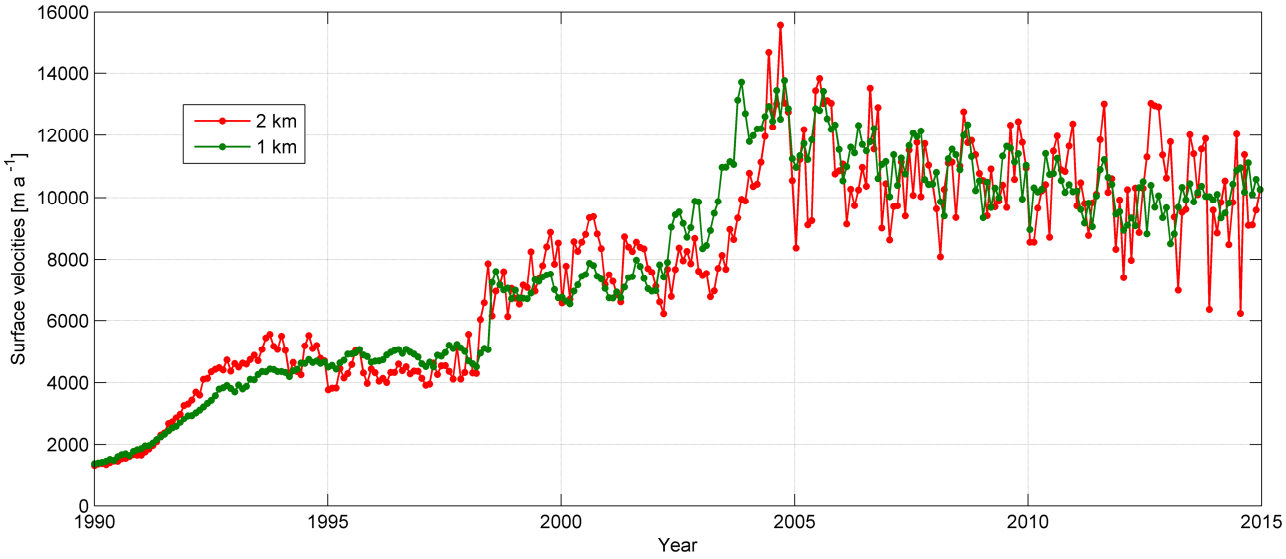

Figure S12. Time series of modelled horizontal velocities on a 2 km and a 1 km grid for the period 1990-2014 at the point location S2 shown in Fig. 1C.

1.3.2 Bedrock topography

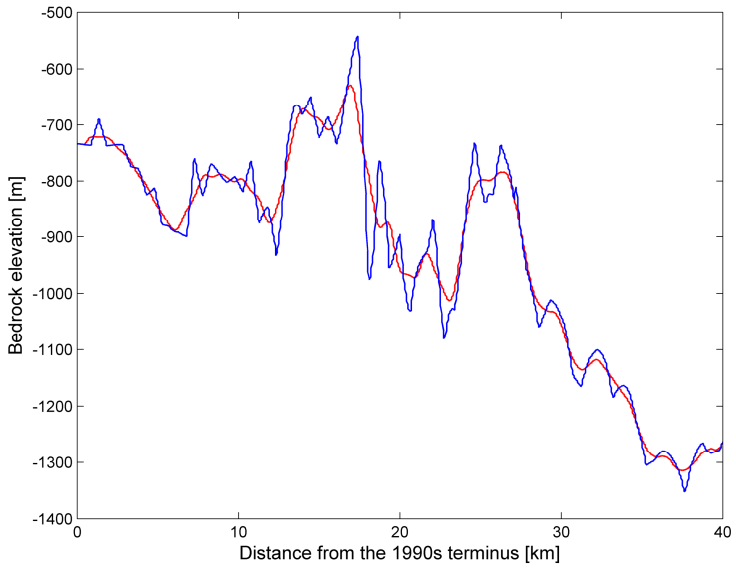

Figure S13. Bedrock elevation (blue line) and smoothed bedrock elevation (red line) (as taken from Bamber et al., 2013) along the flowline showed in Fig. 1C.

1.4 Seasonal variation of the terminus

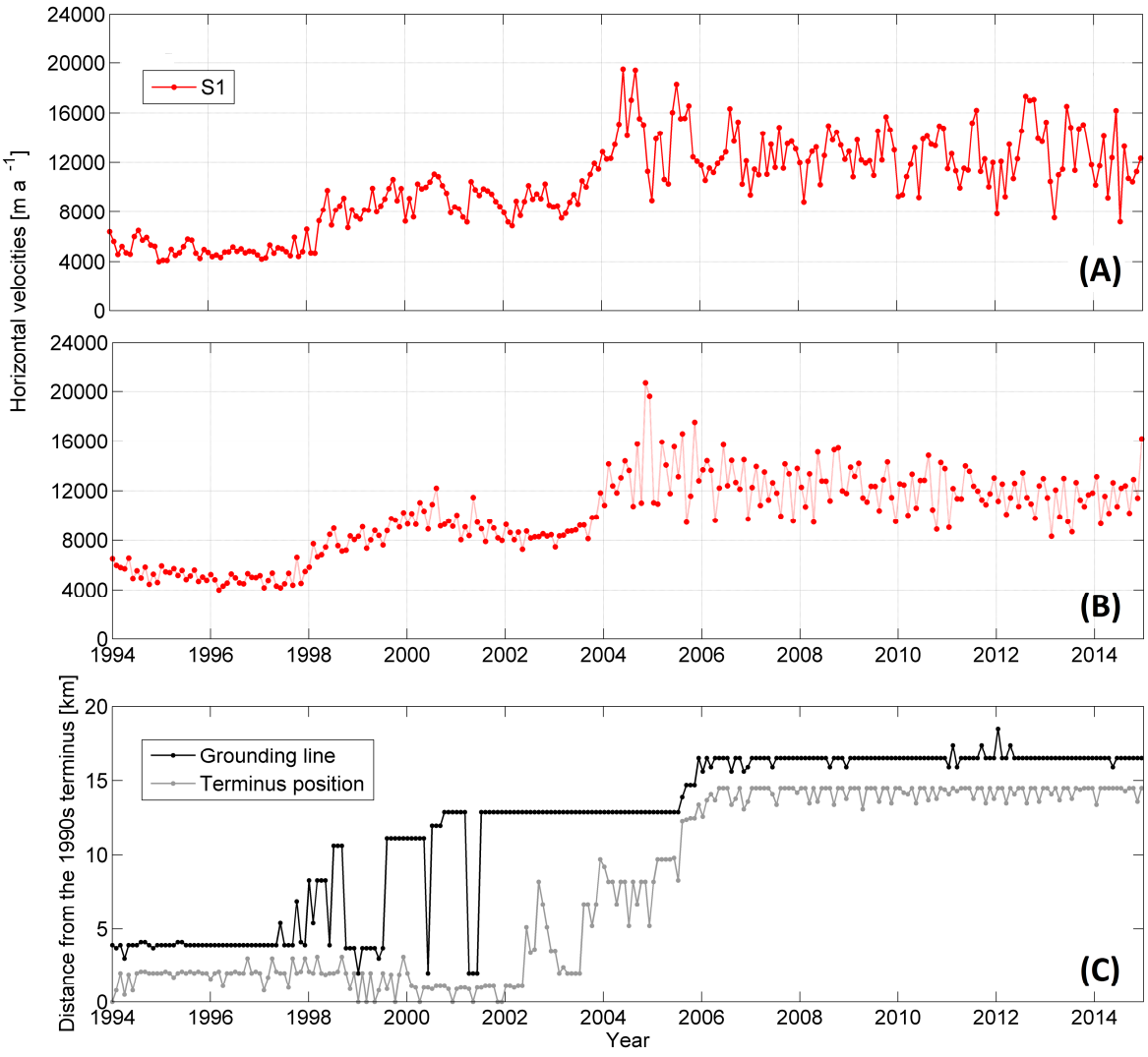

Figure S14. Time series of modelled velocities for the period 1990-2014 at the point location S1 shown in Fig. 1C with monthly climate forcing (i.e. monthly 1990-2014 SMB and temperature) (A) and constant monthly climate forcing (i.e. mean 1960-1990 SMB and temperature) (B). (C) Modelled grounding line and terminus position (ice thickness > 50 m) with constant climatic forcing.

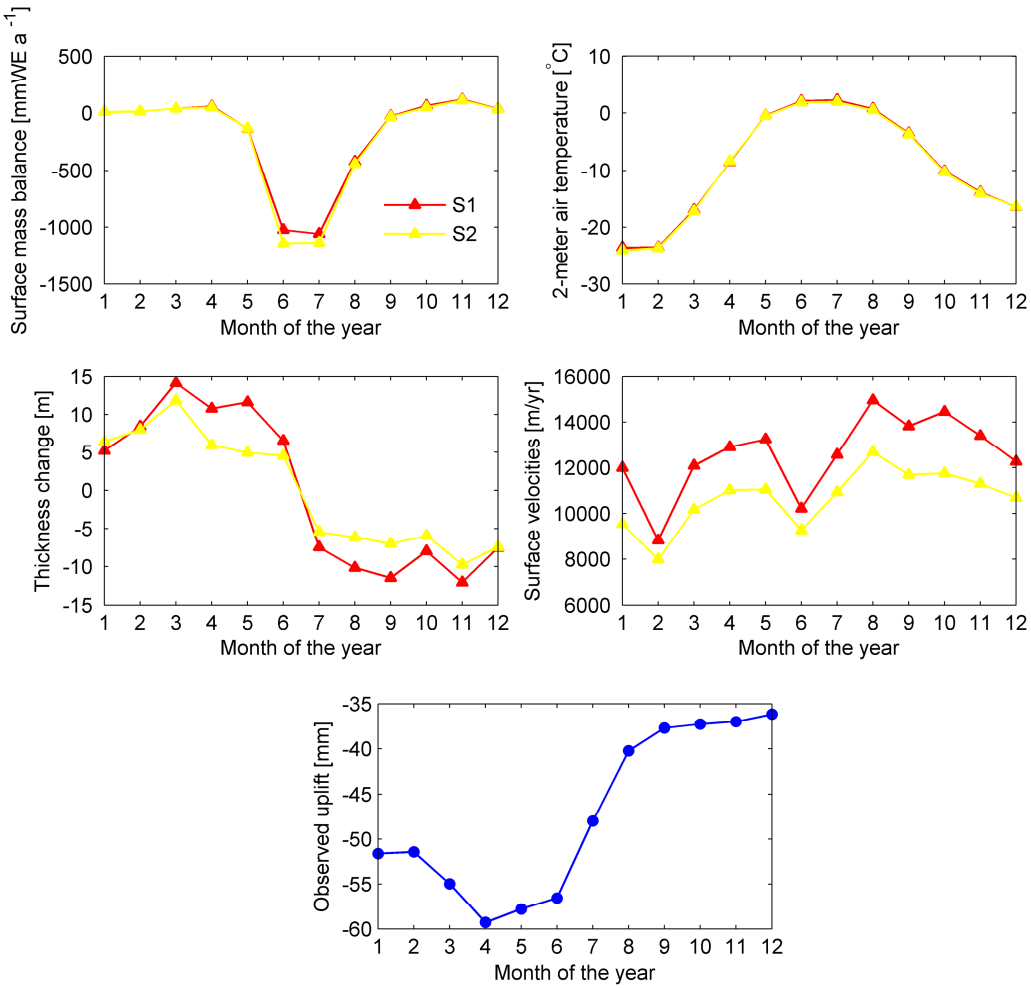

1

2

3 Figure S15. (First row) Monthly surface mass balance [mmWE a-1] and 2-meter air temperature [°C]
4 (Noël et al., 2015) for 2008 in S1 and S2 (see Fig. 1C), (Second row) Modelled monthly thickness
5 changes [m] and surface velocities [m/yr] for 2008 in S1 and S2 (see Fig. 1C), and (Third row)
6 Observed uplift [mm] for 2008 at station KAGA.

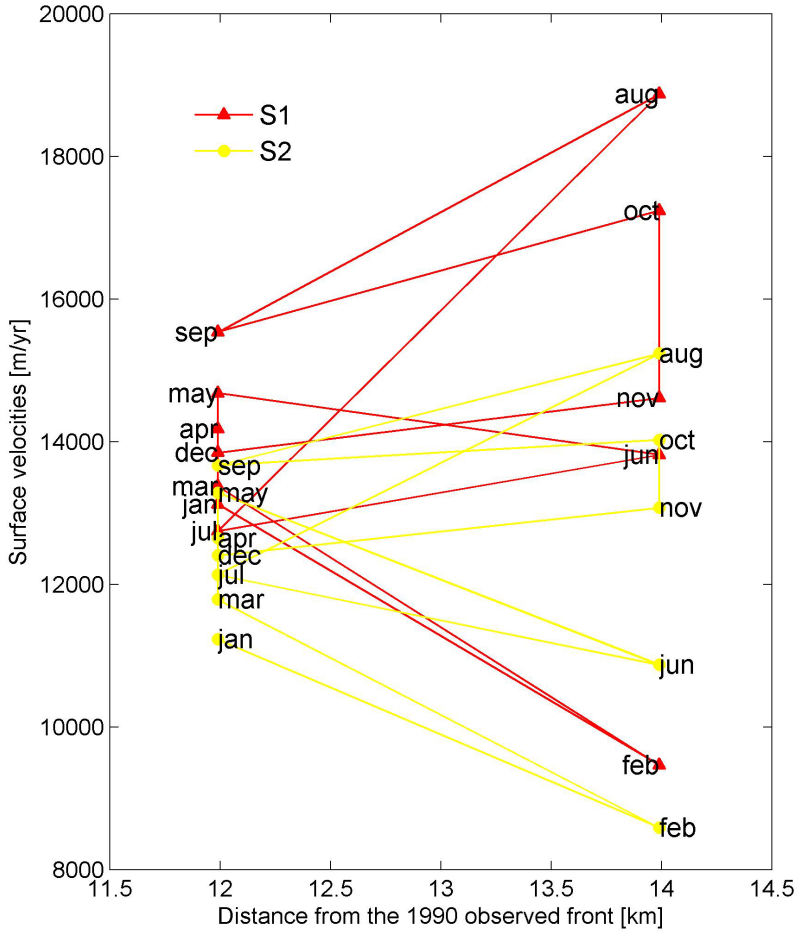

Figure S16. Modelled variation in JIs flow speed for 2008 in S1 and S2 (see Fig. 1C) due to monthly advance and retreat of the terminus.

Figs. 7, S8, S14-S16 show that the overall variability in the modelled horizontal velocities is a response to variations in terminus position.

2 Observed ice mass change

We estimate the rate of ice volume change using 1997–2014 NASA's Airborn Topographic Mapper (ATM) flights (Krabill, 2014) derived altimetry, supplemented with Ice, Cloud and land Elevation Satellite (ICESat) data (Zwally et al., 2012) for 2003–2009 and Land, Vegetation and Ice Sensor (LVIS) data (Blair and Hofton 2012) for 2007–2012, CryoSat-2 data (Wouters et al., 2015) for 2010–2014, and European Remote-Sensing Satellite (ERS-2) data during 1997-2003. ATM flight lines in the

JI region between 1993 and 1996 cover only a minor transect, and are therefore not used. The procedure for deriving ice surface elevation changes is identical to that in Khan et al. (2013) and is similar to the method used by, for example, Ewert et al. (2012) and Smith et al. (2009). However, ice surface elevation changes from cryostat-2 data were derived as described by Wouters et al. (2015) and Helm et al. (2014). We convert the volume loss rate into a mass loss rate and take firn compaction into account as described by Kuipers Munneke et al. (2015). Further, corrections are made for bedrock movement caused by elastic uplift from present-day mass changes (Khan et al., 2010) and long-term past ice mass changes, Glacial Isostatic Adjustment (GIA), (Peltier, 2004). Table 3 shows the ice mass change rates in Gt a^{-1} during 1997-2014.

Table S4. Estimated ice mass change rates in Gt a^{-1} from airborne and satellite laser altimetry for 1997–2014

Time span	Mass change [Gt a^{-1}]
1997–2003	-5.9 ± 2.7
2003–2006	-10.4 ± 1.4
2006–2009	-18.7 ± 1.2
2009–2012	-27.4 ± 1.6
2012–2014	-33.1 ± 2.2

3 Modelled and observed elastic uplift due to mass changes from JI

We assess the mass change from the regional 3-D outlet glacier model by comparing predicted and observed bedrock displacements. We predict displacements by convolving mass change from the regional 3-D outlet glacier model with the Green's function for vertical displacements for the Preliminary Reference Earth Model (Dziewonski and Anderson, 1981) (see Fig. 4 solid black curve).

We compare predicted bedrock displacements with observed displacements from Global Positioning System (GPS) time series at four sites located between 5 and 150 km from the front of JI. To estimate site coordinates from GPS measurements, we follow the procedure of Khan et al. (2010). Fig. 5 (blue curve) shows observed GPS time series of monthly average vertical bedrock displacements caused by the Earth's elastic response to seasonal ice mass variability. To focus on elastic displacements caused by present-day mass variability of the JI, we remove bedrock displacements due to ice mass loss outside JI using load estimates from satellite altimetry (Nielsen et al., 2013) and we remove the GIA based on the deglaciation history ICE-5G (VM2 L90) Version 1.3 estimated by W. R. Peltier.

4 ATM data 1997-1998

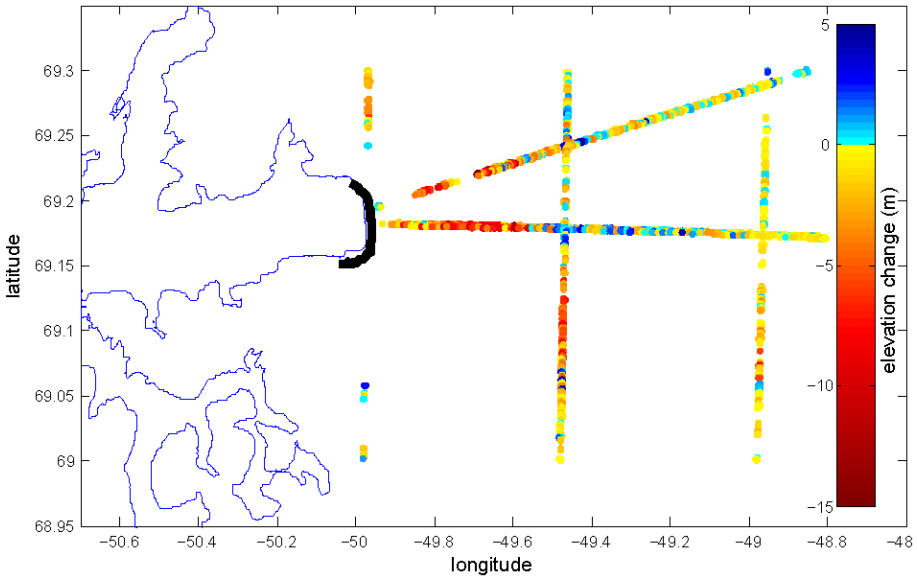

Figure S17. Elevation change from NASA's ATM flights during 1997-1998 at Jakobshavn Isbræ. The thick black line denotes the JI terminus position in 1998. The red and orange circles denote thinning during 1997-1998 both on the northern and southern tributary of JI.

Figure S17 shows thinning during 1997 to 1998. The red circles denote major thinning of ~10 m during 1997-1998 both on the northern and southern tributary of JI.

References

Aschwanden, A., G. Aðalgeirsdóttir, and C. Khroulev. 2013. "Hindcast to measure ice sheet model sensitivity to initial states." *The Cryosphere* 7: 1083–93. doi:10.5194/tcd-6-5069-2012.

Bamber, J. L., J. A. Griggs, R. T. W. L. Hurkmans, J. A. Dowdeswell, S. P. Gogineni, I. Howat, J. Mouginot, et al. 2013. "A new bed elevation dataset for Greenland." The Cryosphere 7: 499–510. doi:10.5194/tc-7-499-2013.

Blair, B., and M. Hofton. 2012. "IceBridge LVIS L2 Geolocated Ground Elevation and Return Energy Quartiles. Boulder, Colorado USA: NASA Distributed Active Archive Center at the National Snow and Ice Data Center. Digital media." http://nsidc.org/data/ilvis2.html.

Dziewonski, A. M., and D. L. Anderson. 1981. "Preliminary reference Earth model." *Physics of the Earth and Planetary Interiors* 25: 297–356. doi:10.1016/0031-9201(81)90046-7.

Cuffey, K. M., and W. S. B. Paterson. 2010. "The Physics of Glaciers". Elsevier, 4th edition. ISBN 9780123694614.

Ewert, H., A. Groh, and R. Dietrich. 2012. "Volume and mass changes of the Greenland ice sheet inferred from ICESat and GRACE." *Journal of Geodynamics* 59-60: 111–23. doi:10.1016/j.jog.2011.06.003.Helm, V. , Humbert, A. and Miller, H. (2014): Elevation and elevation change of Greenland and Antarctica derived from CryoSat-2 , The Cryosphere, 8 (4), pp. 1539-1559 . doi: 10.5194/tc-8-1539-2014.

Feldmann, J., Albrecht, T., Khroulev, C., Pattyn, F., and Levermann, A.: Resolution-dependent performance of grounding line motion in a shallow model compared with a full-Stokes model according to the MISMIP3d intercomparison, J. Glaciol., 60, 353–360, doi:10.3189/2014JoG13J093, 2014.

Gladish, C. V., D. M. Holland, A. Rosing-Asvid, J. W. Behrens, and J. Boje. 2015. "Oceanic boundary conditions for Jakobshavn Glacier. Part I: Variability and renewal of Ilulissat icefjord waters, 2001–2014." Journal of Physical Oceanography 45: 3–32. doi:dx.doi.org/10.1175/JPO-D-14-0044.1.

Khan, S. A., K. H. Kjær, N. J. Korsgaard, J. Wahr, I. R. Joughin, L. H. Timm, J. L. Bamber, et al. 2013. "Recurring dynamically induced thinning during 1985 to 2010 on Upernavik Isstrøm, West Greenland." *Journal of Geophysical Research* 118: 111–21. doi:10.1029/2012JF002481.

Khan, S. A., L. Liu, J. Wahr, I. Howat, I. Joughin, T. van Dam, and K. Fleming. 2010. "GPS measurements of crustal uplift near Jakobshavn Isbræ due to glacial ice mass loss." *Journal of Geophysical Research* 115: B09405. doi:10.1029/2010JB007490.

Krabill, W. B. 2014. "IceBridge ATM L2 Icessn Elevation, Slope, and Roughness, [1993-2014]. Boulder, Colorado USA: NASA Distributed Active Archive Center at the National Snow and Ice Data Center. Digital media.Updated 2014." http://nsidc.org/data/ilatm2.html.

Kuipers Munneke, P., S. R. M. Ligtenberg, B. P. Y Noel, I.M. Howat, J. E. Box, E. Mosley-Thompson, J. R. McConnell, et al. 2015. "Elevation change of the Greenland ice sheet due to surface mass balance and firn processes, 1960–2013." *The Cryosphere Discussions* 9: 3541–80. doi:10.5194/tcd-9-3541-2015.

Martin, M. A., R. Winkelmann, M. Haseloff, T. Albrecht, E. Bueler, C. Khroulev, and A. Levermann. 2011. "The Potsdam Parallel Ice Sheet Model (PISM-PIK), Part II: Dynamical equilibrium simulation of the Antarctic Ice Sheet." The Cryosphere 5: 727–740. doi:10.5194/tc-5-727-2011.

Nielsen, K., S. A. Khan, G. Spada, J. Wahr, M. Bevis, L. Liu, and T. van Dam. 2013. "Vertical and horizontal surface displacements near Jakobshavn Isbræ driven by melt-induced and dynamic ice loss." *Journal of Geophysical Research Solid Earth* 118: 1837–44. doi:10.1002/jgrb.50145.

Noël, B., W. J. van de Berg, E. van Meijgaard, P. Kuipers Munneke, R. S. W. van de Wal, and M. R. van den Broeke. 2015. "Summer snowfall on the Greenland Ice Sheet: a study with the updated regional climate model RACMO2.3." The Cryosphere Discussion 9: 1177-1208. doi: 10.5194/tcd-9-1177-2015.

Peltier, W. R. 2004. "Global glacial isostasy and the surface of the ice-age Earth: The ICE-5G (VM2) model and GRACE." *Annual Review of Earth and Planetary Sciences* 32: 111–49. doi:10.1146/annurev.earth.32.082503.144359.

Petrov, L., and J. P. Boy. 2004. "Study of the atmospheric pressure loading signal in very long baseline interferometry observations." *Journal of Geophysical Research* 109: B03405. doi:10.1029/2003jb002500.

Schoof, C. and R. Hindmarsh. 2010. "Thin-film flows with wall slip: an asymptotic analysis of higher order glacier flow models". Quart. J. Mech. Appl. Math. 63(1): 73–114. doi: 10.1093/qjmam/hbp025.

Smith, B. E., H. A. Fricker, I. R. Joughin, and S. Tulaczyk. 2009. "An inventory of active subglacial lakes in Antarctica detected by ICESat (2003-2008)." *Journal of Glaciology* 55: 573–95. doi:10.3189/002214309789470879.

The PISM Authors. 2014. "PISM, a Parallel Ice Sheet Model." http://www.pism-docs.org.

Wouters, B., A. Martin-Español, V. Helm, T. Flament, J. M. Van Wessem, S. R. M. Ligtenberg, M. R. Van Den Broeke, J. L. Bamber. Dynamic thinning of glaciers on the Southern Antarctic Peninsula. Science, 2015 DOI: 10.1126/science.aaa5727

Winkelmann, R., M. A. Martin, M. Haseloff, T. Albrecht, E. Bueler, C. Khroulev, and A. Levermann. 2011. "The Potsdam Parallel Ice Sheet Model (PISM-PIK) Part 1: Model description." *The Cryosphere* 5: 715–26. doi:10.5194/tc-5-715-2011.

Zwally, H. J., R. Schutz, C. Bentley, J. Bufton, T. Herring, J. Minster, J. Spinhirne, and R. Thomas. 2012. "GLAS/ICESat L2 Antarctic and Greenland Ice Sheet Altimetry Data V031. Boulder, Colorado: NASA Distributed Active Archive Center at the National Snow and Ice Data Center. Digital media."